BNL-113366-2016-JA

The PROSPECT Physics Program

The PROSPECT Collaboration

November, 1, 2016

Physics Department

Brookhaven National Laboratory

DISCLAIMER

The PROSPECT Physics Program

J Ashenfelter[1], A B Balantekin[2], H R Band[1], G Barclay[3],
C D Bass[4], D Berish[5], L Bignell[6], N S Bowden[7], A Bowes[8],
J P Brodsky[7], C D Bryan[3], J J Cherwinka[9], R Chu[10,11],
T Classen[7], K Commeford[12], A J Conant[13], D Davee[14], D Dean[10],
G Deichert[3], M V Diwan[6], M J Dolinski[12], J Dolph[6],
M DuVernois[2], A S Erikson[13], M T Febbraro[10], J K Gaison[1],
A Galindo-Uribarri[10,11], K Gilje[8], A Glenn[7], B W Goddard[12],
M Green[10,*], B T Hackett[10,11], K Han[1,15], S Hans[16], K M Heeger[1],
B Heffron[10,11], J Insler[12], D E Jaffe[6], D Jones[5], T J Langford[1],
B R Littlejohn[8], D A Martinez Caicedo[8], J T Matta[10],
R D McKeown[13], M P Mendenhall[16], P E Mueller[10],
H P Mumm[17], J Napolitano[5], R Neilson[12], J A Nikkel[1],
D Norcini[1], D Pushin[18], X Qian[6], E Romero[10,11], R Rosero[16],
B S Seilhan[7], R Sharma[6], S Sheets[7], P T Surukuchi[8], C Trinh[12],
R L Varner[10], B Viren[6], W Wang[19,14], B White[10], C White[8],
J Wilhelmi[5], C Williams[10], T Wise[1], H Yao[14], M Yeh[16], Y-R Yen[12],
G Z Zangakis[5], C Zhang[6] and X Zhang[8]
(The PROSPECT Collaboration)

[1]Department of Physics and Wright Laboratory, Department of Physics, Yale University, New Haven, CT, USA
[2]Department of Physics, University of Wisconsin, Madison, Madison, WI, USA
[3]High Flux Isotope Reactor, Oak Ridge National Laboratory, Oak Ridge, TN, USA
[4]Department of Chemistry and Physics, Le Moyne College, Syracuse, NY, USA
[5]Department of Physics, Temple University, Philadelphia, PA, USA
[6]Physics Department, Brookhaven National Laboratory, Upton, NY, USA
[7]Nuclear and Chemical Sciences Division, Lawrence Livermore National Laboratory, Livermore, CA, USA
[8]Department of Physics, Illinois Institute of Technology, Chicago, IL, USA
[9]Physical Sciences Laboratory, University of Wisconsin, Madison, Madison, WI, USA
[10]Physics Division, Oak Ridge National Laboratory, Oak Ridge, TN, USA
[11]Department of Physics and Astronomy, University of Tennessee, Knoxville, TN, USA
[12]Department of Physics, Drexel University, Philadelphia, PA, USA
[13]Nuclear and Radiological Engineering Program, Woodruff School of Mechanical Engineering, Georgia Institute of Technology, Atlanta, GA
[14]Department of Physics, College of William and Mary, Williamsburg, VA, USA
[15]Institute of Nuclear and Particle Physics, Shanghai Jiao Tong University, Shanghai, China
[16]Chemistry Department, Brookhaven National Laboratory, Upton, NY, USA
[17]National Institute of Standards and Technology, Gaithersburg, MD, USA
[18]Institute for Quantum Computing and Department of Physics, University of Waterloo, Waterloo, ON, Canada
[19]School of Physics and Engineering, Sun Yat-Sen University, Guangzhou, Guangdong Province, China
*Current Address: Department of Physics, North Carolina State University, Raleigh, NC, USA

Abstract. The Precision Reactor Oscillation and Spectrum Experiment, PROSPECT, is designed to make a precise measurement of the antineutrino spectrum from a highly-enriched uranium reactor and probe eV-scale sterile neutrinos by searching for neutrino oscillations over a distance of several meters. PROSPECT is conceived as a 2-phase experiment utilizing segmented ^{6}Li-doped liquid scintillator detectors for both efficient detection of reactor antineutrinos through the inverse beta decay reaction and excellent background discrimination. PROSPECT Phase I consists of a movable 3-ton antineutrino detector at distances of 7–12 m from the reactor core. It will probe the best-fit point of the ν_e disappearance experiments at 4σ in 1 year and the favored region of the sterile neutrino parameter space at $>3\sigma$ in 3 years. With a second antineutrino detector at 15–19 m from the reactor, Phase II of PROSPECT can probe the entire allowed parameter space below 10 eV^2 at 5σ in 3 additional years. The measurement of the reactor antineutrino spectrum and the search for short-baseline oscillations with PROSPECT will test the origin of the spectral deviations observed in recent θ_{13} experiments, search for sterile neutrinos, and conclusively address the hypothesis of sterile neutrinos as an explanation of the reactor anomaly.

Contents

1 Executive Summary and Background

Recent neutrino experiments have provided a coherent picture of neutrino flavor change and mixing and allowed the precise determination of oscillation parameters in the 3-neutrino model. However, anomalous results in the measurement of the reactor $\bar{\nu}_e$ flux and spectrum have suggested this picture is incomplete and may be interpreted as indicators of new physics. Reactor $\bar{\nu}_e$ experiments observe a ∼6% deficit in the absolute flux when compared to predictions [1, 2]. The observed flux deficit, the "reactor antineutrino anomaly", has led to the hypothesis of oscillations involving a sterile neutrino state with ∼1 eV^2 mass splitting [3, 4, 5] (figure 1). Moreover, measurements of the reactor $\bar{\nu}_e$ spectrum by recent θ_{13} experiments observe spectral discrepancies compared to predictions, particularly at $\bar{\nu}_e$ energies of 5-7 MeV [6, 7, 8] (figure 2), possibility indicating deficiencies in current prediction methods and/or the nuclear data underlying them. The reactor anomaly and the measured spectral discrepancies are open issues in a suite of anomalous results [4] that may hint at revolutionary new physics in the neutrino sector.

The Precision Reactor Oscillation and Spectrum Experiment, PROSPECT [9], is designed to comprehensively address this situation by making a definitive search for $\bar{\nu}_e$ oscillations at short baselines from a compact reactor core while concurrently making a precise $\bar{\nu}_e$ energy spectrum measurement from a highly-enriched uranium (HEU) research reactor.

Simultaneously measuring the relative $\bar{\nu}_e$ flux and spectrum at multiple distances from the core within the same detector provides a method independent of any reactor model prediction for PROSPECT to probe for oscillations into additional neutrino states in the parameter space favored by reactor and radioactive source experiments. PROSPECT covers a unique region of parameter space at the eV-scale that is complementary to current $\bar{\nu}_e$ disappearance limits from Daya Bay and to ν_μ and ν_e oscillation searches in accelerator-based neutrino oscillation experiments. Together, reactor and accelerator experiments, such as the short baseline program at FNAL, define a comprehensive approach to resolving the current anomalous results in neutrino physics and have the potential to make a paradigm-changing discovery. Observation of an eV-scale sterile neutrino would have a profound impact on our understanding of neutrino physics and the Standard Model of particle physics with wide-ranging implications for the physics reach of the planned US-based long-baseline experiment DUNE [10], searches for neutrinoless double beta decay, neutrino mass constraints from cosmology and beyond.

In addition to directly addressing the sterile neutrino interpretation of the reactor anomaly, PROSPECT will also provide new experimental data to test for deficiencies in reactor $\bar{\nu}_e$ flux predictions. By making a high-resolution energy spectrum measurement, PROSPECT will determine if the observed spectral deviations in Daya Bay and other θ_{13} experiments at commercial nuclear power plants persist in a HEU fueled research reactor and provide a precision benchmark spectrum to test and constrain the modeling of reactor $\bar{\nu}_e$ production. The insights gained into the performance of flux prediction methods and the completeness of nuclear data inputs will be valuable for several reasons. A better understanding
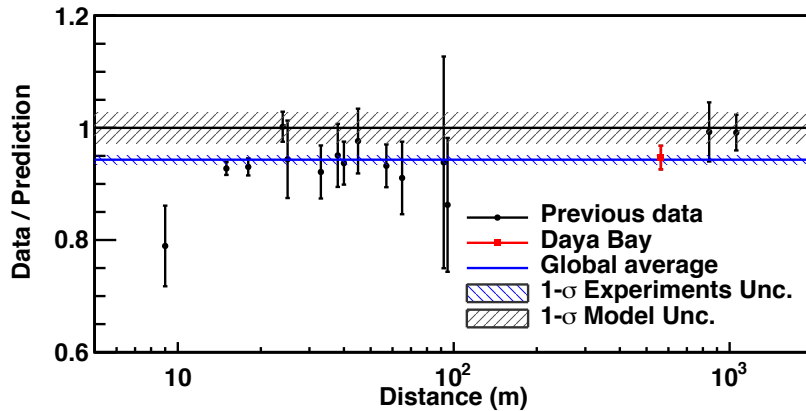

Figure 1. Comparison of measured reactor antineutrino fluxes with predictions based on models for the emission of reactor antineutrinos. The measured deficit relative to prediction is known as the "reactor antineutrino anomaly" [3]. Reprinted figure with permission from [6] Copyright 2016 by the American Physical Society.

of the reactor $\bar{\nu}_e$ spectrum will aid precision medium-baseline reactor experiments such as JUNO and RENO-50 [11], and improve reactor monitoring capabilities for nonproliferation and safeguards.

Therefore, the goals of the PROSPECT experiment are to:

- Make an unambiguous discovery of eV-scale sterile neutrinos through the observations of energy and baseline dependent oscillation effects, or exclude the existence of this particle in the allowed parameter region with high significance. Accomplishing this addresses the proposed sterile neutrino explanation of the reactor anomaly using a method that is independent of reactor flux predictions;

- Directly test reactor antineutrino spectrum predictions using a simple, well-understood reactor system dominated by fission of ^{235}U, while also providing information that is complementary to nuclear data measurement efforts;

- Demonstrate techniques for antineutrino detection on the surface with little overburden;

- Develop technology for reactor monitoring and neutron detection in nonproliferation applications.

PROSPECT will employ a phased approach for the timely exploration of the favored parameter space with the potential of a high-impact discovery while preparing for a definitive measurement across the entire allowed parameter region.
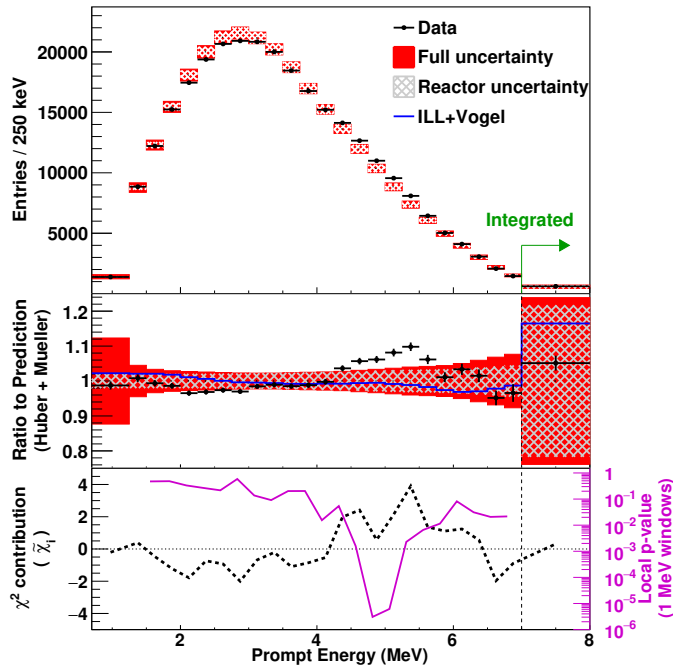
Figure 2. Comparison of the detected prompt energy spectrum observed by Daya Bay to a model-based prediction of pressurized water reactor (PWR) neutrino emission. The deviation from prediction between 4–6 MeV, which is also observed in two other similar experiments, is unexplained and may indicate deficiencies in the models and/or the nuclear data underlying them. Reprinted figure with permission from [6] Copyright 2016 by the American Physical Society.
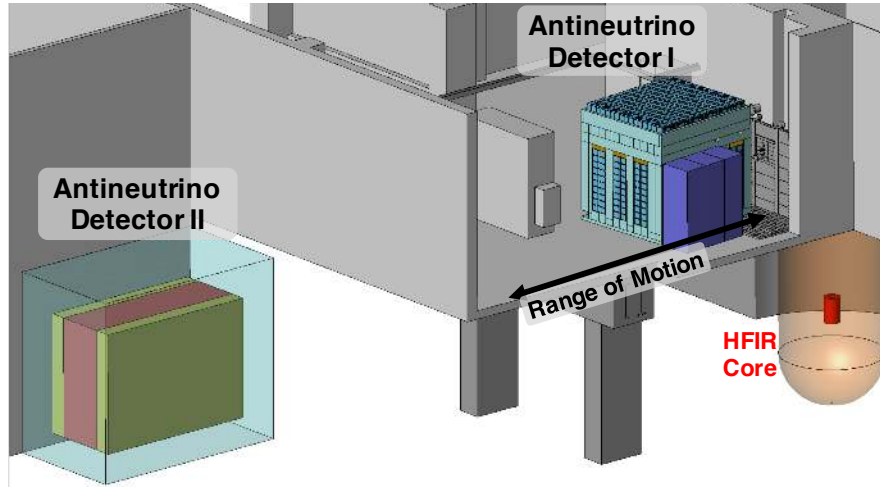
Figure 3. Layout of the PROSPECT experiment. Shown are the HFIR reactor core and the two antineutrino detectors, AD-I and AD-II. Phase I consists of a movable antineutrino detector, AD-I, operated for three years at a baseline range of 7–12 m. Phase II adds a ∼10-ton detector, AD-II, at 15–19 m for an extra three years of data taking.

PROSPECT will be located at the High Flux Isotope Reactor (HFIR) [12] at Oak Ridge National Laboratory (ORNL) [13]. The proposed layout of the experiment is shown in figure 3. Phase I of PROSPECT consists of a ∼3-ton, segmented ^{6}Li-doped liquid scintillator antineutrino detector (AD-I) accessing baselines in the range 7–12 m from the reactor core. Phase II involves the addition of a second ∼10-ton antineutrino detector (AD-II) with identical segmentation spanning baselines between 15–19 m.

PROSPECT combines competitive exposure, baseline mobility for increased physics reach and systematic checks, good energy and position resolution, and efficient background discrimination that yields a signal over background sufficient to achieve the stated goals. The additional second detector in Phase II will significantly improve PROSPECT's sensitivity across the sterile neutrino parameter space. Within a single calendar year, PROSPECT Phase I can probe the best-fit region for all current global analyses of ν_e and $\bar{\nu}_e$ disappearance [4, 5] at 4σ confidence level. Over 3 years of operation, PROSPECT Phase I can discover oscillations as a sign of sterile neutrinos at 5σ for the best-fit point and $>3\sigma$ over the majority of the suggested parameter space. After 3 additional years of operation with a second antineutrino detector in Phase II, essentially all parameter space suggested by ν_e disappearance data below 10 eV^2 can be excluded at 5σ.

1.1 The Reactor Antineutrino Anomaly

Reactor experiments have long played an important role in neutrino physics, using the inverse beta decay (IBD) interaction to detect $\bar{\nu}_e$ emitted by beta decays of fission daughter products. Prior to the discovery of neutrino oscillations, experiments positioned <100 m from a variety of reactor cores, including those at ILL-Grenoble, Bugey, and Savannah River, measured the flux of $\bar{\nu}_e$ with ton-scale detectors based

on liquid scintillators and/or ^{3}He proportional counters [14, 15, 16, 17, 18, 19, 20, 21, 22]. Since these were single detector experiments, it was necessary to compare these observations with predictions of the reactor $\overline{\nu}_e$ flux in order to search for the effect of neutrino oscillation.

Two primary approaches for reactor $\overline{\nu}_e$ flux prediction have been developed. The *ab-initio* method seeks to calculate the flux using tabulated nuclear data and information on the fission rates in a core obtained from reactor neutronics simulations. Neutron-rich fission fragments within a reactor emit $\overline{\nu}_e$ via beta decay with an energy spectrum dependent on the transition between initial and final nuclear states of the particular isotope. The total energy spectrum $S(E_{\overline{\nu}})$ can be expressed as a sum of the decay rate of each unstable isotope i in the reactor, R_i, times the branching fraction for beta decay f_{ij} to the nuclear state j with an energy spectrum $S_{ij}(E_{\overline{\nu}})$,

$$S(E_{\overline{\nu}}) = \sum_i R_i \sum_j f_{ij} S_{ij}(E_{\overline{\nu}}). \tag{1}$$

While this *ab-initio* approach is straightforward in principle, it is complex in practice. More than 1000 unstable isotopes contribute, and many fission yields and individual beta decay spectra are poorly known. For those measured, there can still be significant uncertainty in the decay levels, branching fractions, and $\overline{\nu}_e$ energy spectra. Nonetheless, early attempts at this method [23, 24, 25, 26] aided in the interpretation of contemporary experiments and provided great insight into the $\overline{\nu}_e$ generation processes in reactors. More recently, it has been demonstrated that the two major nuclear databases, ENDF and JEFF, contain differences in branching fractions [27], complicating the interpretation of these calculations. Separately, total-absorption gamma spectroscopy measurements of key isotopes have shown that quoted uncertainties are frequently underestimated [28]. Consequently, *ab-initio* calculations of $S(E_{\overline{\nu}})$ are thought accurate to only $\sim$10% [29].

The second prediction approach, the conversion method, uses precision measurements of the β^- spectrum emitted by fissioning isotopes measured at the ILL-Grenoble research reactor [30, 31, 32, 33]. Using nuclear decay theory, the integral β^- spectrum can be converted to a $\overline{\nu}_e$ spectrum. Again, since nuclear level and decay data are not known for all contributing isotopes a conversion procedure based on iterative fitting of "virtual" beta branches was developed. The advantage of this approach is that the contributions from most fission daughters are included, but with the downside that the conversion process introduces systematic uncertainties. The conversion method predictions were the benchmark against which most experiments were compared during the 1980s and 1990s, and good agreement between measured and predicted fluxes was observed for baselines less than 100 m.

Motivated by experiments seeking to measure θ_{13}, an improved prediction of the reactor $\overline{\nu}_e$ flux was performed [1] using a novel approach combining *ab-initio* and conversion methods, incorporating updated nuclear data, and more accurate nuclear corrections. The summation, or *ab-initio*, portion of the prediction built the $\overline{\nu}_e$ spectrum from the sum of daughter products contributions for which fission yield, branching ratio, and decay information were available from nuclear databases, allowing nuclear corrections to be applied at the branch level. The residual $\sim$10% of the spectrum was derived via a conversion procedure using the reference ILL β^- spectrum [30, 31, 32, 33]. The residual contribution to the total β^- spectra from

fission daughter products isotopes without nuclear data was fit using five virtual β-branches, where importantly and in contrast to past prediction methods, corrections were applied at the branch level. The $\overline{\nu}_e$ spectrum obtained following this approach, when combined with the inverse beta decay cross section, resulted in a systematic increase in the detectable reactor $\overline{\nu}_e$ flux compared to previous predictions. Note that this increase is due to the improved evaluation resulting in a greater proportion of the emitted $\overline{\nu}_e$ being above the threshold for inverse beta decay – the total $\overline{\nu}_e$ flux is still anchored to the normalization of the ILL β^- measurement. In conjunction with the revision of the neutron mean lifetime [34], this effect results in an average deficit of 5.7% in all the short-baseline reactor $\overline{\nu}_e$ measurements. This discrepancy between data and prediction, referred to as the "reactor antineutrino anomaly" [3], represents a deficit in the ratio of observed to expected $\overline{\nu}_e$ from unity significant at 98.6% confidence level.

An independent cross-check was performed using an approach based only on an improved conversion of the ILL reference β^- spectrum, which minimized the use of nuclear databases [2]. Virtual β-branches were used to convert the ILL reference to an $\overline{\nu}_e$ spectrum, yielding a net increase of $\sim$6% in antineutrino predictions, consistent with the flux predicted in [1]. The cause of the increase relative to past predictions was also understood to be due to the use of improved nuclear corrections, the updated neutron lifetime, and the application of corrections to the beta decay spectrum at the branch level, in contrast to the "effective" correction used in past predictions. Additionally, blind analyses from recent kilometer baseline precision rate measurements are consistent with the previous reactor experiments [6, 7, 8]. The disagreement between modern reactor $\overline{\nu}_e$ flux predictions and measurement is therefore well-established.

Neutrino oscillations at short baselines with a mass splitting of $\Delta m^2 \sim 1$ eV^2 have been proposed as one explanation for these observations [3]. With invisible decay width results from Z boson measurements stringently limiting the number of active neutrino flavors to three [34], any additional existing neutrino should be 'sterile' and not participate in weak interactions. The oscillation arising from such a neutrino with eV-scale mass splitting can be observed with a suitable detector located close to a reactor and capable of probing the reactor neutrino flux over a distance of several meters. For baselines >10m the L/E dependent neutrino oscillation will begin to decohere.

Deficiencies in the flux prediction methods and/or imperfections in the measured data underlying them are also viable explanations for the reactor antineutrino anomaly. For example, incomplete nuclear data for the beta decays contributing to the reactor spectrum as well as uncertainties in the corrections applied to individual beta spectra may lead to significant uncertainties in the conversion procedure between the reference beta electron and the emitted $\overline{\nu}_e$ spectra [29].

1.2 Reactor Spectrum Anomaly

In addition to the discrepancy between measured and observed fluxes, recent high-precision measurements of the antineutrino energy spectrum from θ_{13} experiments have shown deviations from the theoretically predicted spectral shapes. The measured energy spectra from Daya Bay, Double Chooz, and RENO each show a $\sim$10% excess of events with energies between 4 and 6 MeV [6, 7, 8], corresponding

to antineutrino energies of ∼5-7 MeV.

Initial studies indicated that the *ab-initio* method reproduced the shape of the spectrum better than the beta-conversion predictions [35]. However, re-analyses with updated fission and beta-branch information call this result into question and instead point to antineutrinos produced by the ^{238}U fission chain as a possible source of the spectral anomaly [27]. New measurements with total-absorption gamma spectrometers at ORNL [36] and University of Jyväskylä [28] will reduce uncertainties in individual beta decay levels and branching ratios. However, predicting antineutrino spectra resulting from these decays remains challenging due to unknown shape corrections. Similarly, uncertainties in the cumulative fission yields are not addressed by these measurements. Precision measurements of reactor antineutrino spectra provide a unique experimental probe that can address many of these questions [27]. In particular, a first-ever precision measurement of the ^{235}U spectrum would highly constrain predictions for a static single fissile isotope system, as compared to commercial power reactors that have evolving fuel mixtures of multiple fissile isotopes [37].

Observed spectral discrepancies in addition to the flux deficit highlight concerns of deficiencies in the flux prediction methods and/or imperfections in the measured data underlying them. More precision experimental data is needed to understand and explain these observations. PROSPECT can address both of these possibilities through a high precision spectral measurement in addition to an oscillation search for sterile neutrinos, and therefore provide a comprehensive resolution of the current "reactor anomalies."

1.3 *Anomalies in Source and Accelerator Experiments*

Anomalous results have also been obtained in other neutrino experiments. Both the SAGE and GALLEX radiochemical gallium experiments have observed neutrino flux deficits with high-activity ν_e calibration sources [38, 39, 40, 41].

Additional anomalies have become apparent in accelerator-based neutrino experiments. The Liquid Scintillator Neutrino Detector (LSND) Experiment at Los Alamos National Laboratory was designed to search for neutrino oscillations in the $\overline{\nu}_\mu \rightarrow \overline{\nu}_e$ channel. It measured an excess of events at low energy consistent with an oscillation mass splitting of $|\Delta m^2|{\sim}1$ eV^2 [42]. The Mini Booster Neutrino Experiment (MiniBooNE) at Fermilab National Accelerator Laboratory was conceived to test this so-called "LSND anomaly" in the same L/E region [43]. In both the $\overline{\nu}_\mu \rightarrow \overline{\nu}_e$ and $\nu_\mu \rightarrow \nu_e$ appearance channels, it observed an excess of events. There is some disagreement regarding the compatibility of MiniBooNE $\overline{\nu}_e$ appearance data in models involving 3 active neutrinos and 1 sterile state (3+1 model) [44] but the allowed regions for neutrino oscillations partially overlap with the allowed regions from LSND.

1.4 *Global Fits*

Attempts have been made to fully incorporate the observed anomalies into frameworks with one or more additional sterile neutrino states. Combining the short-baseline reactor anomaly data with the gallium measurements under the assumption of one additional sterile neutrino state allows one to determine the allowed regions (Δm_{14}^2, $\sin^2 2\theta_{14}$) in the global parameter space. Two recent efforts
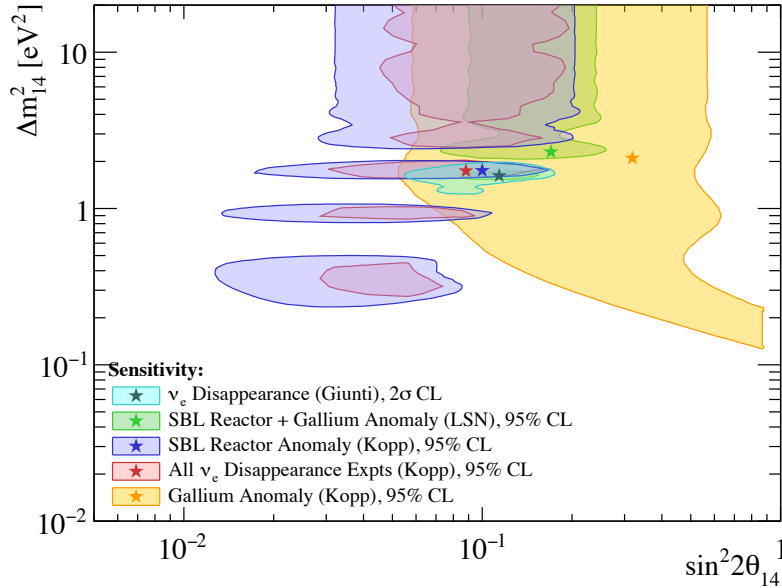
Figure 4. Allowed regions in 3+1 framework for several combinations of ν_e and $\overline{\nu}_e$ disappearance experiments. Contours obtained from [5, 3, 44].

obtain slightly different allowed regions and global best-fit points [5, 3]. The disagreement can be attributed to the differences in handling uncertainties and the choice of spectral information included in the analyses. Inclusion of all ν_e and $\overline{\nu}_e$ disappearance measurements further constrains the parameter space [5]. Figure 4 illustrates the allowed regions obtained from different combinations of anomalous experimental results.

Because of the tensions between some appearance and disappearance results, difficulties arise in developing a consistent picture of oscillations in the 3+1 framework [44] involving both appearance and disappearance data. Efforts at performing a global fit in frameworks containing two additional sterile neutrinos have produced results that have only slightly better compatibility [5]. Excluding the MiniBooNE low-energy excesses yields allowed regions in a 3+1 framework and has been suggested [44] as a "pragmatic approach," based on the observation that the MiniBooNE anomalies cannot be explained in any of the frameworks.

A short-baseline oscillation experiment sensitive to the phase space in Δm_{14}^2 and $\sin^2 2\theta_{14}$ suggested by ν_e and $\overline{\nu}_e$ global fits (see figure 4) will be to able to conclusively address the ~ 1 eV^2 sterile neutrino interpretation of these anomalous results.

2 PROSPECT Physics Program and Discovery Potential

2.1 Sensitivity to Short-Baseline Neutrino Oscillation

PROSPECT will perform a sensitive search for light sterile neutrinos at the eV mass scale by probing signatures of neutrino oscillation through a relative comparison of
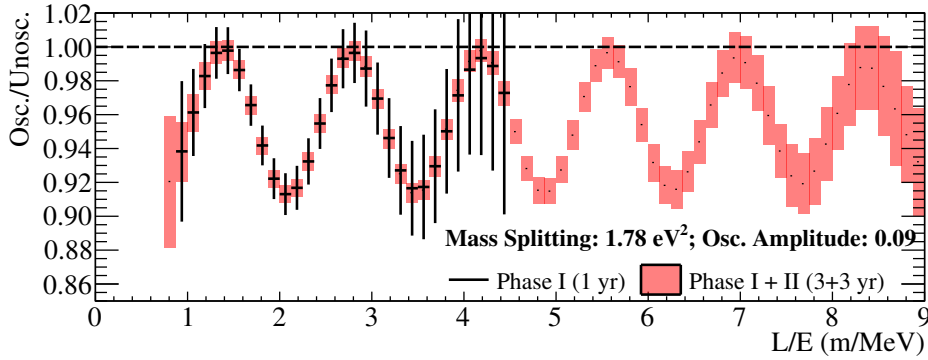
Figure 5. Asymmetry between oscillated and un-oscillated L/E spectra after 1 year of Phase I (black) and 3 years of both Phase I+II for oscillation parameters suggested by the best-fit region.

the reactor flux and spectrum across a range of baselines (figure 3). The experiment has been designed (section 3) to provide significant improvements in baseline coverage, event statistics, and energy resolution over previous short-baseline reactor oscillation measurements, thus providing coverage of oscillation parameter space that was previously inaccessible.

To demonstrate the oscillation physics reach, we present sensitivity studies assuming the existence of one sterile neutrino in addition to the three known neutrino species, commonly referred to as the 3+1 model. We note that PROSPECT's broad baseline range and in particular its extended reach in L/E during Phase II will also provide sensitivity to multiple sterile neutrinos [45]. The choice of many input parameters is informed by the PROSPECT R&D program. This includes detailed information on the HFIR core, AD-I performance and background estimates obtained from simulation studies and test detector operation, and deployment locations based on engineering engagement with the HFIR facility.

PROSPECT will measure the relative $\bar{\nu}_e$ flux and spectrum as a function of reconstructed baseline and can directly map out the oscillation effect within the segmented detectors [47]. This is shown in figure 5 for the single sterile neutrino hypothesis with parameters matching a global fit to ν_e disappearance data (Ref. [5], hereafter referred to as "Kopp best-fit"). For this best-fit mass splitting, more than one full oscillation wavelength will be visible in PROSPECT Phase I due to the wide baseline and energy range covered. Extension of PROSPECT to Phase II accesses more oscillation cycles and adds statistical precision, thereby enhancing sensitivity. It should be emphasized that the oscillation measurement in the PROSPECT AD-I is a relative comparison between L/E bins rather than between the flux measured in each AD-I segment. Each segment contributes to the majority of L/E bins leading to multiple segments contributing to the same oscillation parameter space. Therefore relative normalization plays a less important role in PROSPECT than near and far detector relative normalization does in the recent θ_{13} experiments. Furthermore, as AD-I is moved, the relative contribution of each segment to a particular L/E bin varies, reducing the effect of both correlated and uncorrelated systematic biases more efficiently than a single extended detector.

PROSPECT oscillation sensitivity is determined using a χ^2 minimization [48]. Systematic uncertainties are included by minimizing over nuisance parameters in
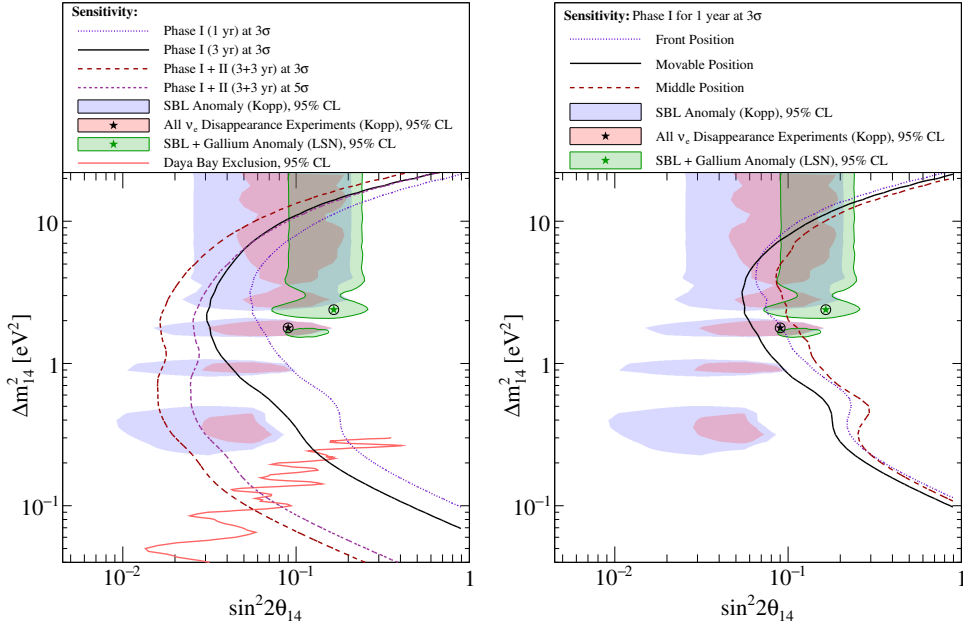
Figure 6. (Left) PROSPECT Phase I and Phase II sensitivities to a single sterile neutrino flavor. Phase I probes the best-fit point at 4σ after 1 year of data taking and has $>3\sigma$ reach of the favored parameter space after 3 years. The combined reach of Phase I+II after 3+3 years of data taking yields a 5σ coverage over the majority of the parameter space below $\Delta m_{14}^2 \sim 10$ eV^2. Daya Bay exclusion curve is from [46]. (Right) Increase in oscillation sensitivity to sterile neutrinos during Phase I by operating AD-I at two positions instead of at the front or middle position only.

addition to the new oscillation parameters (Δm_{14}^2, $\sin^2 2\theta_{14}$). We take a conservative approach by allowing uncertainties for these parameters to vary broadly with little penalty in the fit. Relative uncertainties in normalizations and uncorrelated spectral variations between segments are assigned a 1% uncertainty to match segment-to-segment differences observed in Monte Carlo simulations of the AD-I design. Simulation-predicted signal and background spectra are used (figure 7) and the signal-to-background ratio adjusted to account for the $1/r^2$ flux reduction at farther positions.

The sensitivity of PROSPECT to $\bar{\nu}_e$ oscillation after 1 and 3 calendar years (6 and 18 reactor cycles, respectively) is shown in figure 6. During the first year of data taking, AD-I will be operated for equal times at two positions separated by $\sim$1.5 m. The 3 year run will further increase baseline coverage with deployment at a third location separated by an additional $\sim$1.5 m from the front position. Within a single calendar year, PROSPECT can probe the best-fit of all current global analyses of ν_e and $\bar{\nu}_e$ disappearance [4, 5] at 4σ confidence level. Over 3 years of operation, PROSPECT Phase I can discover oscillations as a manifestation of sterile neutrinos at $>3\sigma$ over the majority of suggested parameter space. The sensitivity achieved with Phase II is also shown: after 3 additional years of operation essentially all parameter space suggested by ν_e disappearance data below 10 eV^2 can be excluded.

The dependence of the sensitivity on experimental parameters is examined in Table 2. These results clearly validate the design focus on background rejection and

Table 1. Nominal PROSPECT experimental parameters. Phase I consists of operating AD-I for three years split between front, middle, and back positions. Phase II adds AD-II at a longer baseline and operates both detectors for three additional years.

Parameter	Value
Reactor	
Power	85 MW
Shape	Cylinder
Size	0.2 m r × 0.5 m h
Fuel	HEU
Duty cycle	41% reactor-on
Antineutrino Detector 1 (AD-I)	
Cross-section	1.2×1.45 m^2
Proton density	5.5×10^{28} p/m^3
Total Target Mass	2940 kg
Fiducialized Target Mass	1480 kg
Baseline range	4.4 m
Efficiency in Fiducial Volume	42%
Position resolution	15 cm
Energy resolution	4.5%/$\sqrt{E/MeV}$
S:B Ratio	3.0, 2.3, 1.7
Closest distance	6.9 m, 8.1 m, 9.4 m
Antineutrino Detector 2 (AD-II)	
Total Target Mass	∼10 ton
Fiducialized Target Mass	∼70%
Baseline range	∼4 m
Efficiency in Fiducial Volume	42%
Position resolution	15 cm
Energy resolution	4.5%/$\sqrt{E/MeV}$
S:B ratio	3.0
Closest distance	15 m
Operational Exposure	
Phase I	1, 3 years
Phase II	3 years

maximizing target mass, while also highlighting the value of covering the widest possible baseline range via movement of AD-I. The increase in sensitivity afforded by the expanded L/E coverage gained though AD-I movement is further illustrated in the right panel of figure 6. Although the signal decreases as $1/r^2$, the gain from L/E coverage surpasses the loss due to reduced signal when the detector is operated equally at two positions. It must be noted that for the sensitivity calculation shown this gain is purely from the improved L/E coverage. Moving the detector also gives a better control of correlated and uncorrelated systematic biases, which can be expected to further increase the sensitivity. The ultimate choice of positions will be guided by the demonstrated signal-to-background performance at various baselines.

Table 2. The effect of varying experimental parameters (*italic*) on the confidence level in the unit of σ with which oscillations at the Kopp best-fit point can be differentiated from the null hypothesis with one year of data-taking.

	Decreased	**Nominal**	**Increased**
Position	*Front only*	*Movable*	*Middle only*
	2.79	4.60	2.37
Position **Resolution**	*10cm*	*14.6cm*	*20cm*
	4.69	4.60	4.46
Efficiency	*32%*	*42%*	*52%*
	3.84	4.60	5.26
Energy **Resolution**	*3%*	*4.5%*	*20%*
	4.61	4.60	4.20
Background **Suppression**	*×0.33*	–	*×3*
	3.92	4.60	5.00
Bin-to-Bin **Uncertainty**	*0.5%*	*1.0%*	*2.0%*
	4.69	4.60	4.30
Relative Segment **Normalization**	*0.5%*	*1.0%*	*2.0%*
	4.60	4.60	4.59
Detector **Size**	*10×8*	*12×10*	*14×12*
	3.23	4.60	6.02

2.2 *Precision Measurement of the Reactor $\overline{\nu}_e$ Spectrum*

PROSPECT will measure the energy spectrum of $\overline{\nu}_e$ emitted by an HEU reactor with a precision that exceeds previous experiments and current model predictions. Between 2–6 MeV, Phase I will achieve an average statistical precision better than 1.5% and systematic precision better than 2%. The target energy resolution, $4.5\%/\sqrt{E/MeV}$, will be greater than any previous reactor experiment and will allow for the detection of fine structure in the antineutrino spectrum. Approximately 60% of the year is reactor-off time that will be utilized to study the rate and shape of cosmogenic backgrounds that mimic IBD events. A Monte Carlo simulation of these backgrounds is shown in figure 7 statistical error bars from the simulation. The measured cosmogenic backgrounds will be subtracted from the antineutrino spectrum, minimizing uncertainties from simulation. Figure 8 shows the projected statistical uncertainties, including background subtraction and assuming 300 keV binning, for Phase I compared to the only published measurement of the ^{235}U neutrino spectrum from Ref. [14]. PROSPECT will significantly improve upon the precision of this measurement throughout the entire IBD range, while extending the measurement to higher energies.

In contrast to LEU reactors where the fission fractions change as plutonium isotopes are produced in the core, HEU reactors produce a static neutrino spectrum simplifying the evaluation of flux prediction models. Figure 9 shows the differences
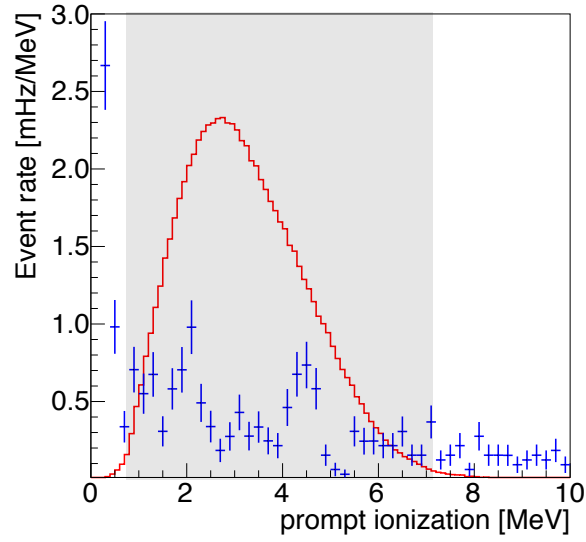
Figure 7. Simulated AD-I IBD signal (red) and background (blue) spectra at near position of AD-I after all analysis cuts. Signal-to-background of better than 1:1 is predicted. Monte Carlo statistical error bars are shown on the simulated background spectrum. The rate and shape of the residual IBD-like background can be measured with high precision during reactor off periods. The shading represents the region of interest for the study of sterile neutrino oscillation and the test of the spectral distortion.
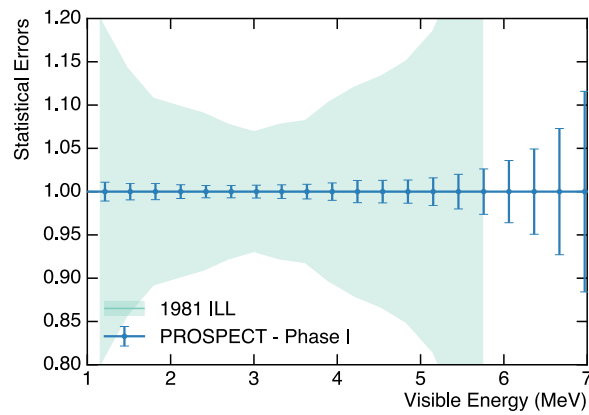

Figure 8. Comparison of PROSPECT Phase I statistical uncertainties, including background subtraction, to the only published ^{235}U spectrum from Ref. [14]. A significant improvement is observed at all energies and the accessible energy range is extended.
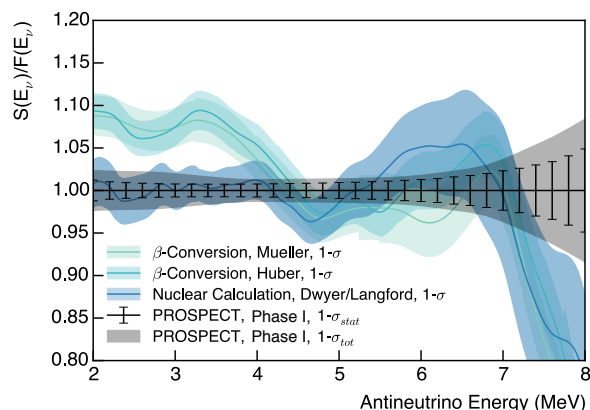
Figure 9. Three models of the ^{235}U $\bar{\nu}_e$ energy spectrum (Mueller [1], Huber [2], and Dwyer/Langford [35]) are shown relative to a smooth approximation. The 1σ error band of the Phase I measurement including subtraction of simulated background (error bars) and systematic uncertainties (gray band) are shown for comparison. An energy resolution of $4.5\%/\sqrt{E/MeV}$ has been applied to highlight accessible features.

between three current models: two based on the β^--conversion method, and one based on *ab-initio* calculation. To highlight the shape differences between models, they are shown in ratio to a smooth approximation $F(E)$‡. The PROSPECT Phase I statistical precision is shown as the black error bars, accounting for subtraction of simulated backgrounds assuming equal exposure of signal and background. PROSPECT will be able to discriminate between these models and directly measure the spectrum more precisely than any of the predictions. In addition, this measurement can be combined with those underway at LEU reactors to extract the non-^{235}U contribution to the spectrum. Since current LEU measurements, and that of HEU which we propose, are expected to have percent-level precision, differences should be prominent and provide another route to evaluate and refine reactor models.

As recently demonstrated by the Daya Bay collaboration, efficient removal of detector response can be achieved through spectral unfolding procedures [6]. Using a simulated detector response model, the incident neutrino energy spectrum may be reconstructed from the detected prompt energy spectrum. Detailed investigations are underway studying the application of these techniques to PROSPECT.

The segmented AD-I detector is designed to enhance the spectral measurement through careful optimization of detector uniformity and construction techniques. The use of low-mass reflector panels, described in more detail in section 5.1, minimizes the non-scintillating volume that could bias the detected energy spectrum. Multiple fiducialization schemes are being studied to determine the optimum volume selection that maximizes detection efficiency of positron annihilation gammas.

AD-II is designed to achieve at least equal statistical power to that of AD-I, even at a longer baseline. A larger target mass and improved cosmogenic shielding increase the IBD detection rate without decreased signal-to-background

‡ $F(E_{\bar{v}}) = \exp(\sum_i \alpha_i E_{\bar{v}}^{i-1})$, with $\boldsymbol{\alpha} = \{1.418, -0.6078, 8.955\times10^{-3}, -6.690\times10^{-3}, 6.933\times10^{-5}\}$
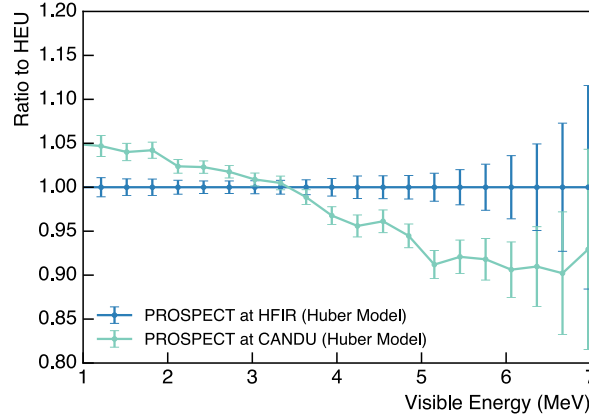
Figure 10. Ratio of 3 year simulated measurements using the model of Huber [2] at HFIR and a CANDU reactor, assuming identical statistics and backgrounds. Only statistical uncertainties are shown, as systematics will cancel. This *time independent* difference in spectra is due to differing fuel mixes.

ratio. Both antineutrino detectors AD-I and AD-II are comprised of identical segments, ensuring that systematic uncertainties will be consistent. Thus, all development and characterization of AD-I will directly apply to AD-II, simplifying the combined analysis during Phase II.

PROSPECT detectors are also uniquely suited to make a detailed study of cosmogenic backgrounds at the Earth's surface and provide valuable input for the design of future near-surface detectors. PROSPECT and its prototype detectors have the ability to measure the variation in the cosmic background rate as the shielding mass and aspect ratio are varied, as well as the relative shielding effectiveness of cost-effective materials, such as water bricks and recycled polyethylene. We will study background rejection and event identification through particle identification cuts, timing cuts, event topology, and fiducialization. These measurements will also allow for the validation of background Monte Carlo simulations with bounded uncertainties. More details about the background studies can be found in Section 5.

2.3 *Applied Physics Measurements*

The PROSPECT experiment will develop technology, produce scientific results, and construct a detector that could find utility in other areas.

While the highest priority for future spectrum measurements are HEU-fueled reactors, examination of other reactor types is also valuable. Measurement of a LEU reactor spectrum with the superior energy resolution of the PROSPECT AD-I would supplement current statistically precise measurements [6, 7, 8], improve the knowledge of $\bar{\nu}_e$ spectra from fission of ^{238}U, ^{239}Pu and ^{241}Pu, and reduce systematic uncertainties in the comparison of LEU and HEU $\bar{\nu}_e$ spectra through use of a common detector for both measurements. Measurement of a CANDU reactor [49, 50], in which frequent refueling maintains a static fuel mixture of ^{235}U, ^{238}U, ^{239}Pu, and ^{241}Pu, would further improve the determination of each spectral component. Reactors with different core neutron spectra, which populate different fission daughter distributions, should also be considered [27]. PROSPECT has
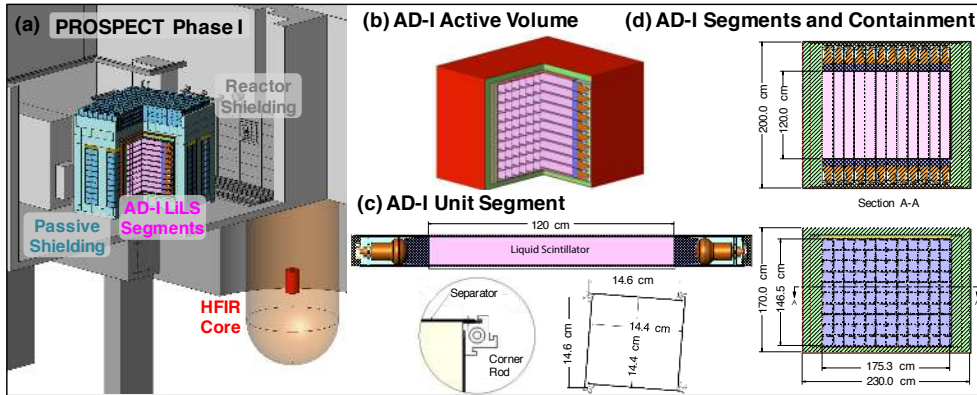
Figure 11. (a) Model of AD-I for Phase I at HFIR. (b) A cutaway diagram of the AD-I. (c) The unit segment structure. (d) Inner and outer dimensions of the AD-I.

contacts at several candidate reactors for such follow-up measurements after its run at HFIR.

Compact $\overline{\nu}_e$ detector development is also of interest for reactor monitoring applications [51, 52, 53]. PROSPECT will advance these efforts through development of background rejection techniques, demonstration of near-surface $\overline{\nu}_e$ detection, and precision $\overline{\nu}_e$ spectrum measurement in compact detectors. These capabilities are of interest to potential end users of reactor monitoring technology [54, 55]. Successful demonstration of reactor $\overline{\nu}_e$ flux and spectrum measurements near-surface would open a range of deployment possibilities that would otherwise be inaccessible.

3 PROSPECT Experimental Strategy

3.1 Reactor Site

After a thorough study of three possible US research reactor sites, all of which could support the experimental goals, HFIR at ORNL was selected for Phase I of PROSPECT. Facility parameters, including the size and power of the compact HEU fueled core, and operational duty cycle are given in Table 1. Deployment locations for both AD-I and AD-II, shown in figure 3, have excellent access and controllable reactor-correlated and cosmogenic background levels. Through extensive engagement with HFIR, it has been established that AD-I and the associated passive shielding design meets all space, floor-loading, and safety requirements and would permit a ∼3 m range of horizontal movement.

Extensive background measurements at AD-I locations have identified specific "hot spots" that can be reduced with localized shielding (section 4.0.1). There is no significant reactor-correlated background at the AD-II location. Prototype detector and shielding tests show that reactor-produced γ-ray and neutron backgrounds can be suppressed to insignificant levels with appropriate shielding (section 4.0.4). Remaining time-correlated backgrounds are dominated by cosmogenic fast neutrons since the detector sites have minimal overburden. Shielding for AD-I will therefore have fixed lead walls to control reactor backgrounds and shielding that moves with the detector to reduce cosmogenic backgrounds.

3.2 *Antineutrino Detector Design and Performance*

The PROSPECT Phase-I antineutrino detector consists of a single volume of ^{6}Li-loaded liquid scintillator (LiLS) segmented by low-mass high-reflectivity optical separators. AD-I detects reactor $\bar{\nu}_e$ via the inverse beta decay reaction $\bar{\nu}_e + p \rightarrow$ e$^+$+n. The positron carries most of the $\bar{\nu}_e$ kinetic energy and makes a prompt energy signal in the LS. The neutron thermalizes before capturing on ^{6}Li or hydrogen, producing a delayed signal $\sim$40 μs later. Neutron captures on ^{6}Li can be identified by the decay products, a back-to-back alpha (α) and triton (t), using pulse shape discrimination-capable LS. The energy deposit is also highly localized in space, allowing for good containment of events in a ton-scale detector. The time-correlated signature of a positron-like prompt signal and a neutron capture delayed signal is an extremely effective handle to eliminate a large majority of randomly time-coincident (accidental) backgrounds.

The optical separators divide the total active volume ($\sim$3000 L) into 120 individual segments (figure 11) providing baseline and event topology information independent of light transport and timing. Each segment shares optical separator panels and hollow support rods with its nearest neighbors and is read out at both ends by photomultiplier tubes (PMTs). Space constraints have largely determined the designed segment length, while cross-section dimensions are constrained by the physical dimensions of the PMTs and their housing assemblies. To maintain LiLS compatibility, the PMT and its voltage divider are housed inside a polycarbonate module with a light guide for optical coupling. Modules are assembled (10 high $\times$ 12 long) to form a support structure for the optical separator array. The separator panels and corner rods are designed to minimize inactive material and amount to 1.8% of the total target mass. This is significantly less than earlier experiments, such as Bugey 3 (15.5% inactive mass) [56]. A carefully selected subset of the support rods house either optical fibers or tubes containing movable radioactive sources to calibrate segment energy response and timing. Cables, fibers, and calibration tubes are routed to the top surface, and this inner detector structure is inserted into a sealed acrylic single-volume LiLS containment vessel that isolates the inner detector from outside moisture and oxygen. All space between PMT modules is filled with LiLS. The inactive LiLS not viewed by PMTs acts as additional passive shielding and totals $\sim$300 L.

The PROSPECT LiLS has been developed over several years to exhibit the light yield needed for the experiment's energy resolution and the pulse shape discrimination (PSD) required for background rejection (section 4.0.2). Enriched ^{6}Li, fluors (PPO) and wavelength shifter (bis-MSB) are added to a commercial scintillator base (EJ-309§ , Eljen Technologies [57]). Prototype studies in a 23 L, 1 m-long, test detector have demonstrated that a detected light yield of 6500 photons per MeV and a bulk attenuation length of 4 m are achievable, leading to an energy resolution of better than $4.5\%/\sqrt{E/MeV}$. The excellent PSD performance demonstrated in section 4.0.3 enables cuts preserving 99.9% of the (n,Li) signal while rejecting the same fraction of γ-ray events.

Detailed simulations based on measured backgrounds at HFIR and perfor-

§ Certain commercial equipment, instruments, or materials are identified in this paper in order to specify the experimental procedure adequately. Such identification is not intended to imply recommendation or endorsement by the National Institute of Standards and Technology, nor is it intended to imply that the materials or equipment identified are necessarily the best available for the purpose.
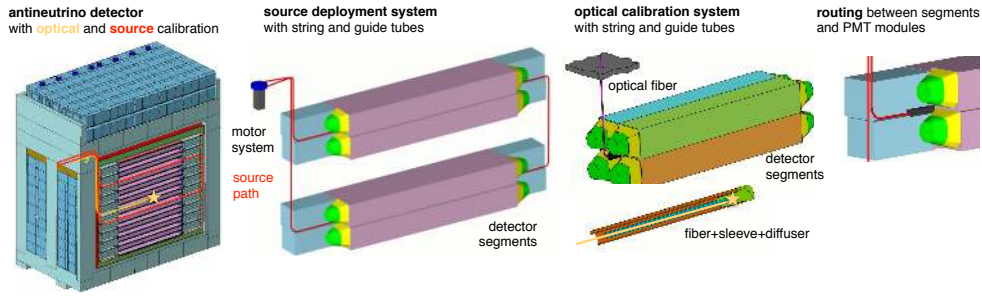
Figure 12. The AD-I source deployment and optical calibration systems. Radioactive sources and an optical system will be deployed between detector segments.

mance of prototypes indicate that PROSPECT can achieve and exceed the required signal-to-background performance of 1:1 (figure 20). Further details are given in section 5.

For Phase II, a second antineutrino detector, AD-II, would be installed just outside the HFIR reactor building covering baselines from 15–19 m. The detector features an increased volume of $\mathcal{O}(10$ tons), while maintaining the same segmentation as AD-I. By using identical segment geometries, systematic uncertainties related to relative detector efficiency can be better controlled and confidence in the projected background rejection is increased. The active detector would be shielded by ~0.75 m of steel and 1 meter of polyetheylene or water (nearly 5 m of water equivalent mass) to reduce cosmogenic backgrounds. Simulations predict a signal-to-background ratio of about 3.0, comparable to the closest AD-I position from the reactor core.

3.3 Calibration Strategy

The segmented AD-I design incorporating hollow support rods will allow extensive access to the full AD-I volume for routine calibration using optical fibers or retractable radioactive sources (figure 12). LiLS light transmission, PMT gain, and PMT timing will be calibrated and monitored with a stabilized pulsed laser source via optical fibers, with each fiber illuminating 4 segments at their midpoint. Encapsulated γ-ray and neutron sources on tensioned string loops will be periodically deployed at multiple locations within the AD-I via Teflon guide tubes in the support rods.

Fitting the deposited energy spectra of radioactive sources will allow the absolute positron energy scale, including scintillator non-linearity, to be calibrated to a few percent or better. These sources can also be used to ensure that small expected differences in positron energy scale between fiducial segments can be characterized to the percent level and corrected for in PROSPECT's sterile oscillation analysis. Neutrons from encapsulated AmBe sources will allow calibration of PSD and determination of neutron detection efficiencies in each segment. Radioactive and cosmogenic backgrounds will be used to monitor and calibrate the detector response between source deployments, following the example of the 23 L test detector, which used ^{40}K, neutron capture on ^{6}Li, and through-going muons. These calibration efforts will allow for the determination of the energy scale to approximately 1% and enable the correction for any time-variation from PMT gain or scintillator

performance.

Finally, the possibility of spiking the scintillator with $\mathcal{O}(10^{-13}$ g) of ^{227}Ac to exploit the double-α cascade from ^{219}Rn$\rightarrow^{215}$Po$\rightarrow^{211}$Pb is being examined. This will allow a measurement of the uniformity per segment to 1% and enable a relative LiLS mass measurement *in-situ*. Further R&D is needed to ensure that dissolution and uniform distribution is possible without introducing unwanted backgrounds.

4 Research and Development Status

The PROSPECT collaboration has conducted a vigorous R&D program since 2013 [48] and is exceptionally well prepared to perform the physics measurements described in section 2. Here we describe the central elements of that R&D program including logistics and background studies at multiple reactors, detector design, liquid scintillator development, prototype operation, and simulation development and validation. Collectively, these efforts demonstrate that the PROSPECT AD-I design for Phase I can be installed in a research reactor facility, meet the necessary performance requirements, and that both reactor-generated and cosmogenic backgrounds can be controlled.

4.0.1 Reactor Facility Background Measurements To obtain the broadest sensitivity to the possible existence of additional neutrino states [47] and to maximize the event rate for a precision $\overline{\nu}_e$ energy spectrum measurement, AD-I must be placed as close to a compact reactor core as possible. In such a location, γ-rays and neutrons produced by reactor operation cannot be neglected, and indeed would be the dominant background source without careful attention to shielding. Furthermore, most facilities have minimal overburden, thus cosmogenic backgrounds are significant relative to the expected signal rate. In particular, fast neutrons from air showers can yield backgrounds that are challenging to shield, either with passive or active approaches.

The PROSPECT collaboration has conducted a careful assessment of natural and reactor generated background radiation that is reported in [58]. These measurements include high and moderate resolution γ-ray spectroscopy, fast and thermal neutron flux, muon flux, and fast neutron spectroscopy. Reactor facilities exhibit significant spatial variation in both γ-ray and neutron backgrounds due to irregular shielding, localized shielding leakage paths, or piping carrying activated materials (figure 13), thus site-specific characterization of background is essential to optimize a shielding design. Localized shielding applied to compact background sources can be a cost- and weight-efficient approach to reducing background. Such an approach has been demonstrated quite successfully at the HFIR site (figure 13). The measurements described in Section 4.0.4 show that targeted shielding, in addition to a carefully designed shielding package, can yield excellent control of reactor related backgrounds.

The flux and spectrum of cosmogenic fast neutrons observed within the minimal overburden provided by the HFIR building is essentially unaltered compared to standard reference measurements (e.g. [59, 60]), which can therefore be used as source terms in simulation studies. The results of these studies have been integral to the design of the Phase I PROSPECT AD-I and have been validated using a series of prototype detectors, as described in Section 4.0.3. The detailed understanding of fast neutron related backgrounds afforded by this work has
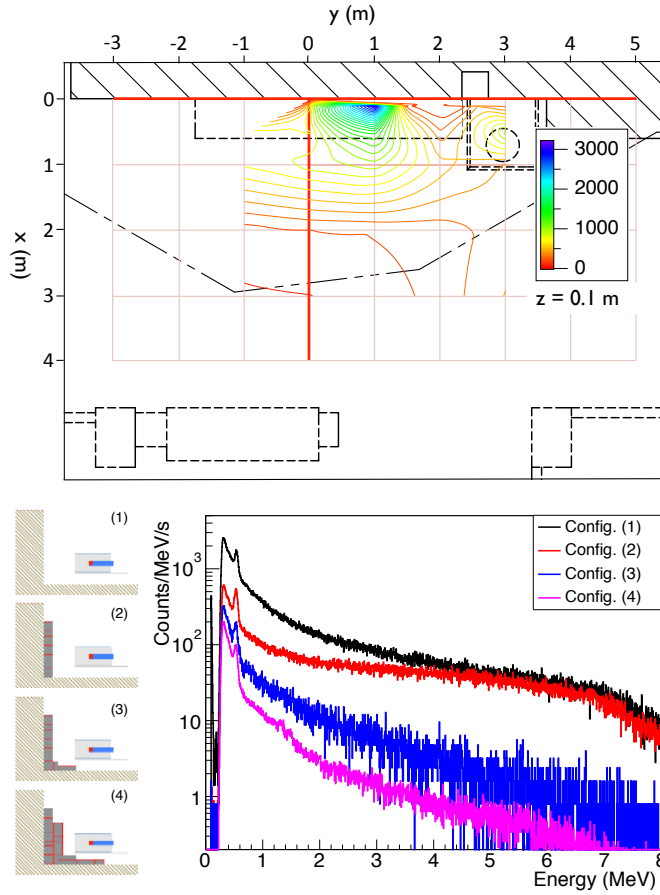
Figure 13. (Top) γ-ray count rates (s^{-1}) for an unshielded 2″ NaI(Tl) detector with HFIR at power. The core is at $(x, y, z) = (-4.06, 0, -3.85)$. Strong spatial variation is caused by a plugged beam tube located at $(x, y, z) = (0, 1, 0)$. (Bottom) Energy spectra for a horizontally collimated 2″ NaI(Tl) detector for varying configurations of a lead wall, with HFIR at power. The shield is centered at the location of highest γ-ray intensity, $(x, y, z) = (0, 1, 0)$. The background rate is significantly reduced, even at high energies. Figure adapted from [58].

enabled the development of a series of effective analysis cuts that yield an expected S:B of better than 1:1, which is discussed in Section 5.

4.0.2 Liquid Scintillator Development Liquid scintillator is the standard detection medium for reactor $\bar{\nu}_e$ detectors due to the high abundance of free proton targets, providing excellent pulse shape discrimination, high light yield, and lower cost than plastic scintillator. Certain types of scintillators have the ability to separate light and heavy charged particle interactions based on their light emission time profiles. This difference allows for the efficient pulse-shape discrimination between electron and proton recoils, improving particle identification and background rejection [61, 62, 63]. Liquid scintillators are frequently loaded with gadolinium to decrease the mean neutron capture time and yield a high-energy capture signal [64].
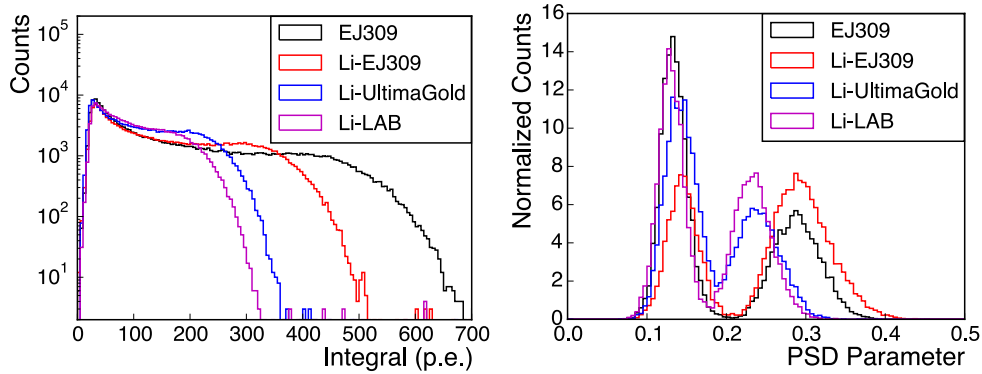
Figure 14. Comparison between unloaded EJ-309 and three different LiLS formulations. (Left) Response to ^{60}Co, demonstrating the relative light yield. (Right) Comparison of PSD distributions when exposed to ^{252}Cf. Li-EJ309 has the best performance amongst Li-loaded materials.

However, gadolinium is ill-suited for use in compact detectors where neutron-capture γ-rays will often escape the active volume. For compact detectors, it is advantageous to incorporate lithium-loading into the LS, as neutron captures on ^{6}Li produce highly localized ($\ll 1$ mm) energy depositions from the reaction $n + ^6\text{Li} \rightarrow \alpha + t + 4.78$ MeV. While the high dE/dx of the alpha and triton results in a quenched light yield (electron equivalent energy of 0.6 MeV$_{ee}$), it also allows discrimination from equivalent-energy electromagnetic backgrounds using the PSD capability of certain liquid scintillators.

Previously available Li-loaded liquid scintillators were based on toxic and flammable solvents that are not suitable for use in reactor facilities. Therefore, a multi-year research and development effort has explored the feasibility of three new low-toxicity and high-flashpoint scintillator bases, LAB, UltimaGold, and EJ-309 [65, 57]. Surfactants are used to form a micro-emulsion containing ^{6}LiCl, creating a dynamically-stable mixture that retains the PSD capability of the base scintillator. Extensive studies were performed with each formulation to characterize light yield and PSD performance using γ-ray and neutron sources.

The EJ-309-based LiLS was found to have the best light yield and PSD performance (figure 14). Li-EJ309 has a proton density of $5.5 \times 10^{22}/\text{cm}^3$, light yield above 6500 photons/MeV, and a bulk attenuation length of $\sim$4 m. The stability of Li-EJ309 samples has been monitored for approximately one year, with the light yield shown to be stable within the 2% measurement uncertainty.

A materials compatibility program studied all components potentially in contact with Li-EJ309 for extended periods of time. The AD-I interior will be constructed only with components that have been qualified, i.e. found to be stable and not degrade LS performance. Acceptable materials include cast acrylic, Teflon, polycarbonate and PLA plastics (clear and colored), Viton, and Acetal.

4.0.3 Detector Prototyping PROSPECT has prototyped many key elements of the proposed AD-I design, including constructing test detectors to validate the light collection efficiency and PSD performance and the low-mass reflector system that optically segments the active liquid scintillator target.
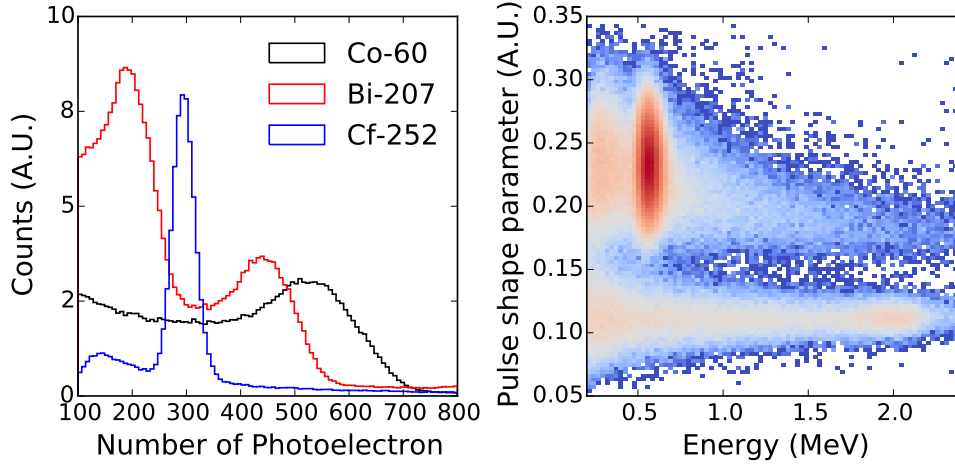
Figure 15. (Left) Measured PE spectra including the Compton edge of ^{60}Co and ^{217}Bi γ-rays and the quenched (n, Li) capture peak from ^{252}Cf neutron source. (Right) PSD performance of Li-EJ309. The upper band is neutron-like events with (n,Li) captures at ≈ 0.6 MeV dominating the statistics. The lower band shows γ-like events.

An acrylic test detector (15 cm × 15 cm × 1 m), referred to as "PROSPECT-20", was produced to validate the performance of the AD-I optical design. The effects of different PMT models, single versus double-ended readout, reflector types, and coupling methods have been explored and reported in [62]. As shown in figure 16, the final configuration of the detector utilized internal reflectors similar to the low-mass panels discussed below and the R6594 PMTs chosen for AD-I [66]. Filled with 23 L of EJ-309 [57], a light collection of 841±17 photoelectrons (PE)/MeV was observed with excellent PSD performance: a rejection factor of 10^4 for γ-rays was achieved while preserving 99.9% of the (n,Li) capture signal between 0.5–0.7 MeV. In addition, both PSD and light collection were found to be totally uniform along the length of the cell within systematic and statistical uncertainties. Position reconstruction along the long-axis of PROSPECT-20 utilizing light arrival time differences between PMTs was also demonstrated with a 5 cm resolution.

When filled with LiLS, an average light collection of 522±16 PE/MeV was measured with three γ-ray sources in the range 0.38–2.0 MeV (figure 15). The demonstrated PE/MeV exceeds the goal of 500 PE/MeV needed to achieve the target $4.5\%/\sqrt{E/MeV}$ energy resolution. Excellent uniformity and PSD performance was again demonstrated at the (n,Li) capture peak and above (figure 15) enabling preservation of 99.9% of the (n,Li) signal while rejecting the same fraction of γ-ray events. The mean neutron capture time is observed to be 40 μs.

For the optical segmentation system, low-mass reflector panels have been developed by adhering 3M Enhanced Specular Reflector (ESR) [67] to both sides of a rigid 0.6 mm thick carbon fiber sheet, and then enclosing this assembly in a Teflon sleeve via heat bonding. The result is a large area, low-mass, highly reflective assembly that is hermetic and liquid scintillator-compatible. A structural support system, described in section 3.2, was prototyped using polycarbonate and 3D-printed white PLA plastic, which allowed for rapid fabrication and testing cycles. A nine-segment mechanical mock-up of the structure has been used to
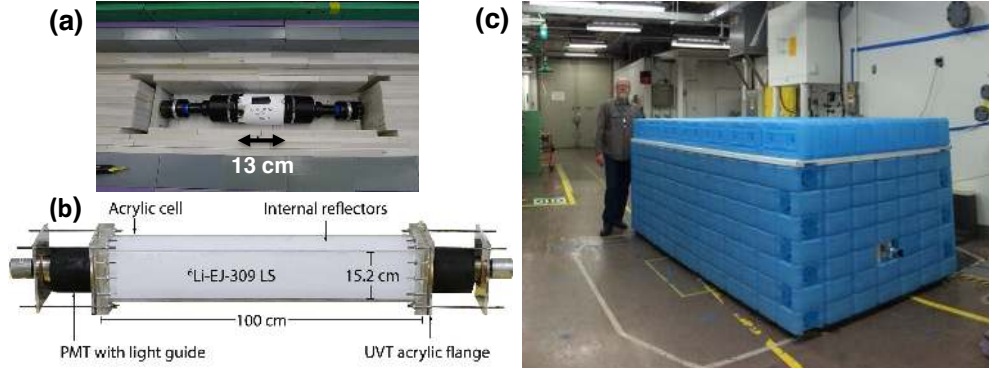
Figure 16. Prototype detectors and shielding installed at the HFIR experimental location. (a) The PROSPECT-2 prototype within a partially assembled polyethylene and lead shield. (b) The PROSPECT-20 prototype with internal reflectors added after operation at HFIR. (c) The PROSPECT-20 shielding enclosure at HFIR.

develop assembly procedures and demonstrate the mechanical robustness of the segmentation system.

4.0.4 Onsite Prototype Detector Operation and Simulation Validation PROSPECT has deployed multiple liquid scintillator prototype detectors and shielding packages at HFIR since mid-2014 to characterize backgrounds *in-situ* and develop a working knowledge of facility regulations, operating procedures and work control processes. Detector size was increased by a hundredfold, from an initial 100 mL EJ-309 cell to a 23 L cell containing LiLS (PROSPECT-20). The shielding packages have likewise grown from a small lead brick cave to a multi-layered shield of water bricks [68], high density polyethylene (HDPE), 5% borated HDPE and lead with a total volume nearly 1/4 that of the proposed AD-I design (figure 16).

Data have been collected over nine months through multiple reactor cycles. Analysis cuts were developed to isolate IBD-like events and elucidate the event types that produce background at this location. The time separation (figure 17 Left) spectrum between prompt and delayed signals is dominated by a random background that is constant in time, but also exhibits an exponentially decaying time-correlated component consistent with that observed for correlated particle processes that terminate in a neutron capture. IBD is one such process (prompt e^+ followed by neutron capture), as are correlated backgrounds due to fast neutron recoil followed by capture or capture of multiple spallation neutrons.

Application of a simple energy cut around the (*n*,Li) capture peak for the delayed signal in an event pair reduces the random component by a factor of 2.8, demonstrating, in part, the utility of LiLS for a compact detector. Applying selections based upon PSD provides further information: requiring that the prompt signal fall in the neutron recoil band indicates that the majority of time-correlated background events in PROSPECT-20 are due to fast neutron recoils followed by capture. Finally, applying selections consistent with IBD events, prompt PSD in γ-like band, delayed signal in (*n*,Li) energy and PSD region, reduces the initial coincidence rate by a factor of 55 and reveals the IBD-like background to be dominated by time-correlated pairs. Accidental coincidences due to reactor-

produced γ-rays following this selection are minimal due to the selectivity of the ^{6}Li neutron capture signature and targeted shielding applied to background "hot-spots" at HFIR. Comparison of IBD-like event energy spectra with the reactor on and off (figure 17 Right) indicates that IBD-like backgrounds are cosmogenic and that reactor generated backgrounds are negligible. The slight increase in events during the reactor-off period is either a statistical fluctuation or could be related to variation in the cosmogenic background rates from seasonal changes. As this is only a single module, the background rate surpasses the expected rate of IBD events.
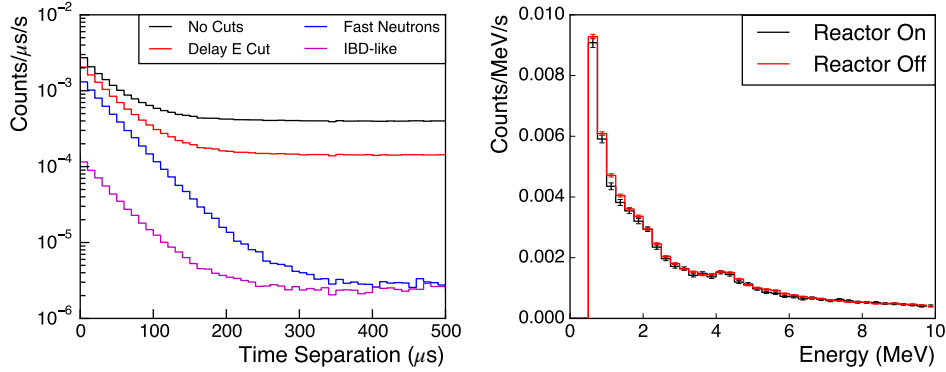

Figure 17. (Left) Time separation between prompt and delayed signals (black) for reactor-off operation of PROSPECT-20 with different analysis cuts applied: delay energy (red), fast neutrons (blue), and IBD-like (purple). (Right) Comparison of PROSPECT-20 IBD-like event prompt energy spectra with HFIR on (black) and off (red).

5 Predicted Detector Response: Signal and Background

A comprehensive and flexible Monte Carlo simulation of the PROSPECT detector design has been developed using the GEANT4 package [69]. Particle interactions are based on the "QGSP_BERT_HP" physics list in GEANT4.10.01p1, which focuses on "high precision" models for lower-energy neutron interactions. Optical photon generation and tracking is optionally available for light transport modeling. The simulation includes geometries for prototype test detectors and the two ADs. A variety of event generators are available, including inverse beta decay, CRYv1.7 [70] for cosmic ray shower generation, a parametrized model for the surface cosmic neutron spectrum [71], and calibration sources.

5.1 Response to the Reactor $\overline{\nu}_e$ Signal

Simulation studies have been used to study the response of the PROSPECT AD-I design to the inverse beta decay signal and many classes of background events. This includes particle transport studies using GEANT4 and examination of segment optical response using both GEANT4 and the SLitrani package [72]. Exploratory studies of segment response confirmed that the choice of an efficient specular reflector, with a component of total internal reflection (TIR) from the Teflon layer encapsulating the segment wall, provided good collection efficiency and uniformity
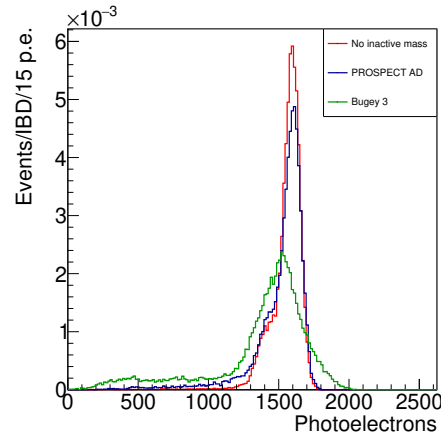
Figure 18. Simulated response to 4 MeV e^+ for AD-I configurations with no inactive mass (red), the PROSPECT low mass optical separators (blue), and an inactive mass fraction equivalent to Bugey 3 (green).

along the entire segment volume. Good agreement was found with the data from the PROSPECT-20 detector using various reflector and light guide configurations.

The response to the e^+ produced by IBD is of particular interest and has been examined for a wide range of segment size, segment wall compositions, and optical configurations. The e^+ response achieved with the AD-I design described above is illustrated in figure 18, which includes both particle and optical scintillation photon transport. Here, the response to mono-energetic 4 MeV positrons distributed uniformly throughout the fiducial detector volume is examined for several segment wall configurations: walls with infintesimal thickness (no inactive mass in active volume), the AD-I design, and a thickness equivalent to that used in the segmented Bugey-3 $\overline{\nu}_e$ detector [73]. The AD-I configuration of low-mass separators has comparable performance to a detector without inactive material and is significantly better than the segmented Bugey 3 detector.

5.2 Backgrounds from Cosmogenic Activity

Data collected using the PROSPECT-20 detector at HFIR have been used to validate the PROSPECT AD-I simulation. For example, figure 19 displays an absolute comparison between data and simulation of cosmic ray shower backgrounds. Both the energy and time distributions of IBD-like events are in good agreement, with the results being consistent with fully explaining the observed IBD-like rate in PROSPECT-20. Although the IBD-like background rate is higher than the expected $\overline{\nu}_e$ interaction rate, improved shielding and cuts possible in the full AD-I will suppress backgrounds substantially, achieving a signal-to-background ratio of ≥ 1 according to simulation.

The validated simulation package indicates that measured IBD-like background in PROSPECT-20 is primarily due to high-energy (tens to hundreds of MeV) cosmic neutrons, with small additions from muon interactions and accidental γ-ray coincidences. These mechanisms are also projected to be the primary source of IBD-
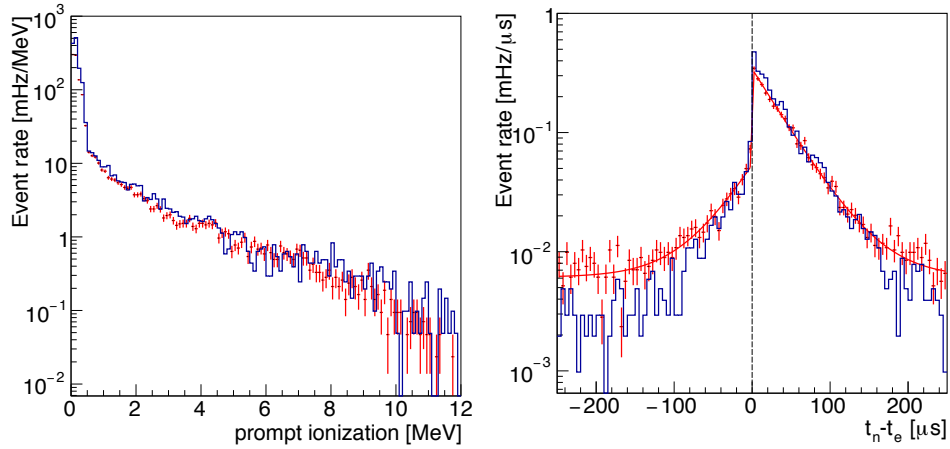
Figure 19. (Left) PROSPECT-20 IBD-like energy distributions from reactor-off data (red) compared to simulation for cosmic backgrounds (blue). (Right) PROSPECT-20 IBD-like timing distributions from reactor-off data (red) compared to simulation for cosmic backgrounds (blue).
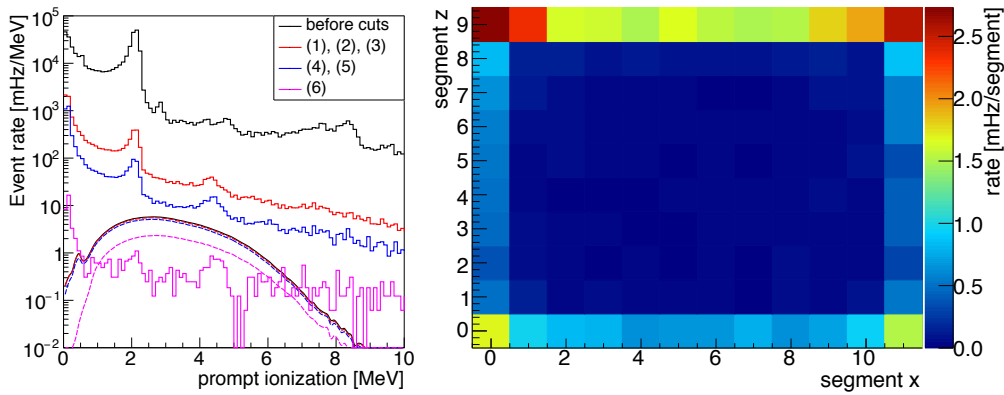

Figure 20. (Left) Simulated AD-I IBD signal and background spectra. Signal (dashed) and background (solid) prompt spectra are shown through selection cuts described in the text. Background is primarily produced by cosmogenic fast neutrons. The signal and background spectra after all cuts are also plotted in figure 7 in linear scale. (Right) Event rates for neutron capture from cosmic background in different segments. The rates are after all non-fiducialization cuts and fiducialization cut along segment length.

like background events in the PROSPECT AD-I. By design, the multi-segment AD-I provides information useful for identifying and vetoing most cosmic background events. However, high-energy cosmic neutrons, which can penetrate undetected deeply into the active volume before inelastic scattering interactions, can produce time-correlated prompt ionization, highly quenched nuclear recoils, and delayed secondary neutron capture signals, and are projected to be the main background source. The rates of cosmogenically-produced ^{9}Li and ^{8}He, which also mimic IBD signals, are estimated to be roughly two orders of magnitude below the IBD rate, and can be measured with reactor-off data. Cosmogenic backgrounds are expected

Table 3. Simulated signal and cosmic background rates in events per day, total Phase I statistics in parentheses, in the energy range $0.8 \leq E \leq 7.2$ MeV, after applying background rejection cuts. Details of each cut are provided in the text.

Cuts	IBD signal		Cosmic BG	
Exposure	*Daily*	*Phase I*	*Daily*	*Phase I*
PSD	1630	7.3e5	2.1e6	9.5e8
Time (1, 2, 3)	1570	7.1e5	3.4e4	1.5e7
Spatial (4, 5)	1440	6.5e5	9900	4.5e6
Fiducial (6)	660	3.0e5	250	1.1e5

to vary with atmospheric, solar, and seasonal conditions. The time-variation of IBD-like background event rates will be studied in detail during reactor off periods along with correlations to fast neutron event rates. Tracking of fast neutron event rates and other cosmogenic backgrounds that do not mimic IBD events will allow for properly normalized background subtraction.

After identification of candidate prompt and delayed signals via deposited energy and PSD selections, additional cuts on event topology (including both time and position information) provide two to three orders of magnitude in background suppression. Figure 20 demonstrates the effectiveness of topology cuts at rejecting cosmic ray background relative to the IBD signal.

The event selections are as follows. "Time topology" cuts include: (1) delayed capture must occur within 100 μs of the prompt ionization; (2) multiple hits in the prompt cluster must occur within 5 ns to reject slower-moving neutron recoil events; (3) events must be isolated from other neutron recoils or captures in a ± 250 μs window, to reject multi-neutron spallation showers. "Spatial topology" cuts include: (4) the prompt and delayed signals must be proximate; (5) multiple segment hits in the prompt signal must be distributed over a compact volume, rejecting extended minimum ionizing tracks and many high-energy gammas; (6) events occurring outside the inner fiducial volume ($\geq$ one segment width from any active volume surface) are vetoed. Expected effects of these cuts on signal and background in the AD-1 detector is shown in figure 20 (Left). Figure 20 (Right) demonstrates the fiducialization effects on the AD-I detector. Event rates of neutron capture from cosmic background after non-fiducialization cuts $1 - 5$ and fiducialization cut along segment length are shown. The outermost layer of segments, where the background rates are much higher, are rejected by fiducialization cuts. Event selection will be optimized and further validated using initial reactor-off data from AD-I.

Although fiducialization decreases the effective active volume for true IBDs by $\sim$50%, it provides a more than tenfold boost in background rejection. Predicted rates with cuts are given in Table 3. Within the fiducialized volume, IBD detection efficiency is 42%. Efficiencies for the fiducial segments are largely consistent: a percent-level 1σ deviation in efficiencies between segments can be corrected for in an oscillation analysis utilizing gamma and neutron calibration results. Monte Carlo investigations have also characterized the small expected geometry-induced spectral
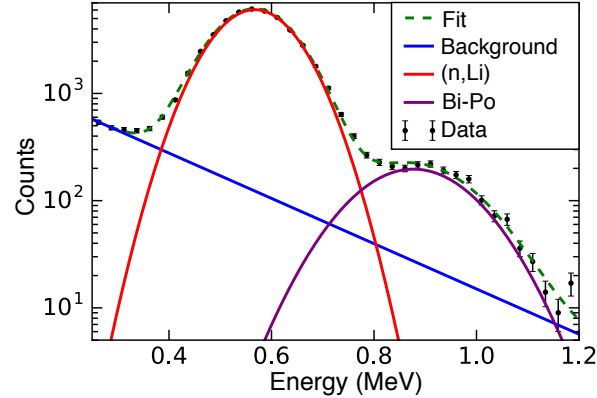
Figure 21. Fitted distribution of delayed energy depositions in the PROSPECT-20 detector collected at HFIR. The main peak is from neutron captures on ^{6}Li, while the smaller peak at 0.89 MeV is from Bi-Po alpha decays. With demonstrated improvements in energy resolution, these peaks will be completely separated in PROSPECT

differences between segments within the fiducialized volume.

While event selection is not yet optimized, the signal-to-background ratio indicated is more than sufficient to meet the PROSPECT physics goals (section 2.1). Although the background prediction is inherently uncertain (estimated to be accurate within a factor of 2), we are confident likely gains from optimization will ensure that PROSPECT can successfully control backgrounds. The simulated background spectrum shown in figure 20 is used in the sensitivity calculations described in section 2. Reactor-off periods will be used to measure the background spectrum directly.

5.3 Backgrounds from Internal Radioactivity

Internal contamination of trace radioactivity can introduce backgrounds that cannot be effectively removed through fiducialization. These predominantly consist of ^{40}K and the uranium and thorium decay chains. Radio-pure materials well-suited for installation in the detector package have been identified. Acrylic and other plastic polymers have largely been demonstrated to be low-background by many experiments, including Daya Bay and other θ_{13} experiments. The internal reflectors are designed to be low-mass and will mainly consist of carbon fiber, another established low-background material. Radioactivity from the PMTs will be mitigated by a combination of passive shielding from inactive light guides and active fiducialization along the segment length using event position reconstruction.

While few radioactive decays produce correlated signals that can mimic the IBD event signature, correlated ^{214}Bi $\rightarrow$ ^{214}Po $\rightarrow$ ^{210}Pb decays in the ^{238}U decay chain are an important exception. Bi-Po decays consist of a beta-decay with endpoint of approximately 3 MeV followed by a 7.8 MeV alpha decay with a half-life of 164 μs. Data collected with PROSPECT-20 at HFIR, shown in figure 21, demonstrate how Bi-Po decays appear in the PROSPECT data stream.

A rate of Bi-Po events of 3.0 ± 0.15/day/liter was observed with the delayed

alpha's quenched light output of 0.89 MeV$_{ee}$. With the demonstrated energy resolution of PROSPECT-20, the alpha peak will be well-separated from the (n,Li) capture peak, eliminating greater than 99.5% of the Bi-Po events while preserving greater than 99% of neutron captures. Applying this rejection power, the Bi-Po signal is reduced to approximately 30/day, an order of magnitude below the IBD rate.

6 Conclusions

Since their first observation some 60 years ago, reactor antineutrinos have been an important tool for the study of neutrino physics. PROSPECT will continue to exploit this unique $\overline{\nu}_e$ source to make a precise measurement of the reactor antineutrino spectrum from ^{235}U with an energy resolution of better than 4.5% at the High Flux Isotope Reactor at ORNL and to search for neutrino oscillations as a sign of eV-scale sterile neutrinos. Utilizing a single, segmented 3-ton liquid scintillator detector located at 7–12 m from the reactor core, PROSPECT Phase I will probe the favored region of neutrino oscillation parameter space at $>3\sigma$ within 3 years of data taking. Phase II will add a second detector with ∼10-tons active target mass and cover the majority of the allowed parameter space at 5σ.

By designing an experiment that can simultaneously make oscillation and spectrum measurements, PROSPECT will be able to address the proposed interpretations of the current 'reactor anomalies:' the existence of sterile neutrinos and/or deficiencies in our ability to predict reactor $\overline{\nu}_e$ emissions. As well as having the potential to make a beyond-the-Standard-Model discovery, PROSPECT has the ability to improve our understanding of antineutrino emission in nuclear reactors. PROSPECT has performed extensive R&D on detector components, while also building and operating a series of test detectors that have allowed the characterization and validation of the detector design as well as background studies in the reactor environment at HFIR. PROSPECT is technically ready to proceed with the construction of the experiment and high impact physics results can be obtained within 1 year of data taking.

7 Acknowledgements

References

[1] Mueller T *et al.* 2011 *Phys. Rev.* **C83** 054615 (*Preprint* `1101.2663`)
[2] Huber P 2011 *Phys. Rev.* **C84** 024617 (*Preprint* `1106.0687`)
[3] Mention G *et al.* 2011 *Phys. Rev.* **D83** 073006 (*Preprint* `1101.2755`)
[4] Abazajian K, Acero M, Agarwalla S, Aguilar-Arevalo A, Albright C *et al.* 2012 (*Preprint* `1204.5379`)
[5] Kopp J, Machado P A N, Maltoni M and Schwetz T 2013 *JHEP* **1305** 050 (*Preprint* `1303.3011`)
[6] An F P *et al.* (Daya Bay) 2016 *Phys. Rev. Lett.* **116** 061801 (*Preprint* `1508.04233`) URL `http://dx.doi.org/10.1103/PhysRevLett.116.061801`

[7] Abe Y *et al.* (Double Chooz) 2014 *JHEP* **10** 086 [Erratum: JHEP02,074(2015)] (*Preprint* `1406.7763`)

[8] Kim S B 2015 *Nucl. Part. Phys. Proc.* **265-266** 93–98 (*Preprint* `1412.2199`)

[9] *PROSPECT website* `http://prospect.yale.edu`

[10] Gandhi R, Kayser B, Masud M and Prakash S 2015 *JHEP* **11** 039 (*Preprint* `1508.06275`)

[11] Capozzi F, Lisi E and Marrone A 2015 *Phys. Rev.* **D92** 093011 (*Preprint* `1508.01392`)

[12] *High Flux Isotope Reactor* `https://neutrons.ornl.gov/hfir`

[13] *Oak Ridge National Laboratory* `https://www.ornl.gov`

[14] Kwon H *et al.* (ILL Collaboration) 1981 *Phys. Rev.* **D24** 1097–1111

[15] Zacek G *et al.* (CALTECH-SIN-TUM) 1986 *Phys. Rev.* **D34** 2621–2636

[16] Vidyakin G S *et al.* (Krasnoyarsk) 1987 *Sov. Phys. JETP* **66** 243–247 [Zh. Eksp. Teor. Fiz.93,424(1987)]

[17] Afonin A I *et al.* (Rovno) 1988 *Sov. Phys. JETP* **67** 213–221 [Zh. Eksp. Teor. Fiz.94N2,1(1988)]

[18] Kuvshinnikov A A *et al.* (Rovno) 1991 *JETP Lett.* **54** 253–257 [Sov. J. Nucl. Phys.52,300(1990)]

[19] Declais Y, Favier J, Metref A, Pessard H, Achkar B *et al.* 1995 *Nucl.Phys.* **B434** 503–534

[20] Declais Y *et al.* (Bugey) 1994 *Phys. Lett.* **B338** 383–389

[21] Vidyakin G S *et al.* (Krasnoyarsk) 1994 *JETP Lett.* **59** 390–393 [Pisma Zh. Eksp. Teor. Fiz.59,364(1994)]

[22] Greenwood Z D *et al.* (SRP) 1996 *Phys. Rev.* **D53** 6054–6064

[23] Davis B, Vogel P, Mann F and Schenter R 1979 *Phys. Rev.* **C19** 2259–2266

[24] Vogel P, Schenter G, Mann F and Schenter R 1981 *Phys. Rev.* **C24** 1543–1553

[25] Klapdor H V and Metzinger J 1982 *Phys. Rev. Lett.* **48** 127–131

[26] Klapdor H V and Metzinger J 1982 *Phys. Lett.* **B112** 22–26

[27] Hayes A C, Friar J L, Garvey G T, Ibeling D, Jungman G, Kawano T and Mills R W 2015 *Phys. Rev.* **D92** 033015 (*Preprint* `1506.00583`)

[28] Zakari-Issoufou A A *et al.* (IGISOL) 2015 *Phys. Rev. Lett.* **115** 102503 (*Preprint* `1504.05812`)

[29] Hayes A C *et al.* 2014 *Phys. Rev. Lett.* **112** 202501 (*Preprint* `1309.4146`)

[30] Schreckenbach K, HR F, Von Feilitzsch F, AA H *et al.* 1981 *Phys. Lett.* **B99** 251

[31] Von Feilitzsch F, Hahn A and Schreckenbach K 1982 *Phys. Lett.* **B118** 162–166

[32] Schreckenbach K, Colvin G, Gelletly W and Von Feilitzsch F 1985 *Phys. Lett.* **B160** 325–330

[33] Hahn A *et al.* 1989 *Phys. Lett.* **B218** 365–368

[34] Olive K *et al.* (Particle Data Group) 2014 *Chin. Phys. C* **38** 090001

[35] Dwyer D A and Langford T J 2015 *Phys. Rev. Lett.* **114** 012502 (*Preprint* `1407.1281`)

[36] Rasco B C *et al.* 2015 *JPS Conf. Proc.* **6** 030018

[37] Buck C, Collin A P, Haser J and Lindner M 2015 (*Preprint* `1512.06656`)

[38] Anselmann P *et al.* (GALLEX) 1995 *Phys. Lett.* **B342** 440–450

[39] Hampel W *et al.* (GALLEX) 1998 *Phys. Lett.* **B420** 114–126

[40] Abdurashitov J *et al.* (SAGE) 1999 *Phys. Rev.* **C59** 2246–2263 (*Preprint* `hep-ph/9803418`)

[41] Abdurashitov J, Gavrin V, Girin S, Gorbachev V, Gurkina P *et al.* 2006 *Phys. Rev.* **C73** 045805 (*Preprint* `nucl-ex/0512041`)

[42] Aguilar-Arevalo A *et al.* (LSND) 2001 *Phys. Rev.* **D64** 112007 (*Preprint* `hep-ex/0104049`)

[43] Aguilar-Arevalo A *et al.* (MiniBooNE) 2013 *Phys. Rev. Lett.* **110** 161801 (*Preprint* `1207.4809`)

[44] Giunti C, Laveder M, Li Y and Long H 2013 *Phys. Rev.* **D88** 073008 (*Preprint* `1308.5288`)

[45] Heeger K, Littlejohn B and Mumm H 2013 (*Preprint* `1307.2859`)

[46] An F P *et al.* (Daya Bay) 2014 *Phys. Rev. Lett.* **113**(14) 141802

[47] Heeger K, Littlejohn B, Mumm H and Tobin M 2013 *Phys. Rev.* **D87** 073008 (*Preprint* `1212.2182`)

[48] Ashenfelter J *et al.* (PROSPECT) 2013 PROSPECT - A Precision Reactor Oscillation and Spectrum Experiment at Short Baselines *Community Summer Study 2013: Snowmass on the Mississippi (CSS2013) Minneapolis, MN, USA, July 29-August 6, 2013* (*Preprint* `1309.7647`)

[49] Boczar P 2012 CANDU nuclear reactor designs, operation and fuel cycle *Nuclear Fuel Cycle Science and Engineering* Woodhead Publishing Series in Energy ed Crossland I (Woodhead Publishing) pp 278 – 299 ISBN 978-0-85709-073-7 URL `http://www.sciencedirect.com/science/article/pii/B9780857090737500118`

[50] Torgerson D, Shalaby B A and Pang S 2006 *Nuclear Engineering and Design* **236** 1565 – 1572 ISSN 0029-5493

[51] Bernstein A, Wang Y F, Gratta G and West T 2002 *J. Appl. Phys.* **91** 4672 (*Preprint* `nucl-ex/0108001`)

[52] Bernstein A *et al.* 2010 *Science and Global Security* **18** 127 (*Preprint* `nucl-ex/0908.4338`)

[53] Jocher G *et al.* 2013 *Phys. Rept.* **527** 131 (*Preprint* `1307.2832`)

[54] IAEA 2009 *Final Report of the Focused Workshop on Antineutrino Detection for Safeguards Applications* sTR-361

[55] IAEA 2012 *Proceedings of the first meeting of the Ad Hoc Working Group on Safeguards Applications utilizing Antineutrino Detection and Monitoring* sG-EQ-GNRL-RP-0002

[56] Achkar B *et al.* 1995 *Nuclear Physics B* **434** 503 – 532 ISSN 0550-3213 URL `http://www.sciencedirect.com/science/article/pii/055032139400513E`

[57] *Eljen EJ-309 Liquid Scintillator* `http://www.eljentechnology.com/index.php/products/liquid-scintillators/73-ej-309`

[58] Ashenfelter J *et al.* (PROSPECT) 2016 *Nucl. Instrum. Meth.* **A806** 401–419 (*Preprint* `1506.03547`)

[59] Gordon M *et al.* 2004 *IEEE Trans. Nucl. Sci.* **51** 3427–3434 ISSN 0018-9499

[60] Kowatari M *et al.* 2005 *J. Nucl. Sci. Technol.* **42** 495–502

[61] Roush M, Wilson M and Hornyak W 1964 *Nuclear Instruments and Methods* **31** 112 – 124 ISSN 0029-554X URL `http://www.sciencedirect.com/science/article/pii/0029554X64903337`

[62] Ashenfelter J *et al.* (PROSPECT) 2015 *JINST* **10** P11004 (*Preprint* `1508.06575`)

[63] Zaitseva N, Glenn A, Martinez H P, Carman L, Pawelczak I *et al.* 2013 *Nucl. Instrum. Methods* **A729** 747

[64] Buck C and Yeh M 2016 *Journal of Physics G: Nuclear and Particle Physics* **43** 093001 URL `http://stacks.iop.org/0954-3899/43/i=9/a=093001`

[65] *PerkinElmer UltimaGold AB Liquid Scintillator* `http://www.perkinelmer.com/catalog/family/id/ultima+gold+ab`

[66] *Hamamatsu Photomultiplier Tubes and Assemblies* `http://www.hamamatsu.com/resources/pdf/etd/High_energy_PMT_TPMO0007E.pdf`

[67] *3M ESR Datasheet* `http://multimedia.3m.com/mws/media/380802O/vikuititm-esr-msds.pdf?fn=ESR.pdf`

[68] *WaterBrick International* `http://www.waterbrick.org`

[69] Agostinelli S *et al.* (GEANT4) 2003 *Nucl. Instrum. Methods* **A506** 250–303

[70] Hagmann C, Lange D and Wright D 2007 Cosmic-ray shower generator (CRY) for Monte Carlo transport codes *Nuclear Science Symposium Conference Record* vol 2 (IEEE) pp 1143–1146

[71] Sato T and Niita K 2006 *Radiat. Res.* **166** 544–555

[72] *Slitrani Optical Simulation Package* `http://gentitfx.fr/SLitrani/`

[73] Abbes M *et al.* 1996 *Nucl. Instrum. Methods* **A374** 164–187